

# Enhanced Photoconductivity at Dislocations in SrTiO<sub>3</sub>

Maximilian Kissel, Lukas Porz, Till Frömling, Atsutomo Nakamura, Jürgen Rödel, and Marin Alexe\*

Dislocations are 1D crystallographic line defects and are usually seen as detrimental to the functional properties of classic semiconductors. It is shown here that this not necessarily accounts for oxide semiconductors in which dislocations are capable of boosting the photoconductivity. Strontium titanate single crystals are controllably deformed to generate a high density of ordered dislocations of two slip systems possessing different mesoscopic arrangements. For both slip systems, nanoscale conductive atomic force microscope investigations reveal a strong enhancement of the photoconductivity around the dislocation cores. Macroscopic in-plane measurements indicate that the two dislocation systems result in different global photoconductivity behavior despite the similar local enhancement. Depending on the arrangement, the global photoresponse can be increased by orders of magnitude. Additionally, indications for a bulk photovoltaic effect enabled by dislocation-surrounding strain fields are observed for the first time. This proves that dislocations in oxide semiconductors can be of large interest for tailoring photoelectric functionalities. Direct evidence that electronic transport is confined to the dislocation core points to a new emerging research field.

## 1. Introduction

So far, great efforts have been made for classical semiconductors to avoid dislocations, which are 1D crystallographic line defects. In these materials, they lead to additional charge carrier scattering and thus a significant reduction of the carriers' mobility. Hence, dislocations negatively affect the targeted functional properties, and great efforts are paid to avoid them. The situation is different in the field of semiconducting oxide ceramics, where purposefully introduced dislocations can be beneficial for functional properties.<sup>[1]</sup>

Fundamental studies of dislocation-mediated basic properties are afforded by tilt and twist bi-crystal interfaces.<sup>[2,3]</sup> If we wish to move beyond these 2D systems to achieve high dislocation densities in the bulk, plastic deformation is a viable approach. However, most ceramics are brittle with limited or no potential for plastic deformation.

Nevertheless, some ceramics have been plastically deformed as single crystals even at room temperature, with MgO,<sup>[4]</sup> SrTiO<sub>3</sub>,<sup>[5]</sup> and ZnS<sup>[6,7]</sup> as examples. However, a fundamental understanding of large-scale plasticity in ceramics is by far missing, and therefore, the investigation into specific functional properties endowed by dislocation networks is in its infancy.

Dislocation cores with their attendant space charge regions and strain fields can provide enhanced functional properties,<sup>[8]</sup> such as ionic or electronic conductivity,<sup>[9,10]</sup> oxygen diffusion,<sup>[11,12]</sup> and enable new functionalities.<sup>[13,14]</sup> Very recent advancements highlight the control of polarization by mechanical dislocation imprint in piezoelectric ceramics<sup>[15]</sup> and creation of low-dimensional superconductivity in SrTiO<sub>3</sub> single crystals.<sup>[16]</sup>


Semiconducting oxides with their high localized charge at the dislocation core<sup>[17,18]</sup> are expected to provide additional states in the band gap affording to tune optical and photoelectric properties. If bulk materials are considered, additional tunability is provided if the oriented mesoscopic dislocation structure is utilized.<sup>[19]</sup> Furthermore, dislocations carry large strain gradients around their cores, which can locally break the inversion symmetry leading to flexoelectric polarization<sup>[20]</sup> and potentially enabling the flexo-photovoltaic effect.<sup>[21]</sup> These features designate dislocations in oxide semiconductors as promising means to enable new photoelectric functionalities.

M. Kissel, M. Alexe  
Department of Physics  
University of Warwick  
Coventry CV4 7AL, UK  
E-mail: m.alex@warwick.ac.uk

M. Kissel, L. Porz, T. Frömling, J. Rödel  
Department of Materials and Earth Sciences  
Technical University of Darmstadt  
64287 Darmstadt, Germany

L. Porz  
Department of Materials Science and Engineering  
Norwegian University of Science and Technology  
Trondheim 7034, Norway

A. Nakamura  
Department of Mechanical Science and Bioengineering  
Osaka University  
1-3 Machikaneyamacho, Toyonaka, Osaka 560-8531, Japan

 The ORCID identification number(s) for the author(s) of this article can be found under <https://doi.org/10.1002/adma.202203032>.

© 2022 The Authors. Advanced Materials published by Wiley-VCH GmbH. This is an open access article under the terms of the Creative Commons Attribution License, which permits use, distribution and reproduction in any medium, provided the original work is properly cited.

DOI: 10.1002/adma.202203032

Dislocations in semiconductor compounds were already investigated in the 1970s, partly concerning photoelectric properties.<sup>[22]</sup> Photoconductivity was found to be decreased in ZnSe single crystals while being deformed,<sup>[23]</sup> which was explained by a concurrent reduction of the Hall mobility<sup>[24]</sup> during plastic deformation. In contrast, after deformation, increased photoconductivity in ZnSe was observed stemming from an additional deep level in the band gap which was attributed to dislocations.<sup>[25]</sup> Illumination was assumed to increase the negative charge on the dislocations by exciting electrons from the valence band into electronic states of the dislocation core.<sup>[26]</sup> Similarly, an additional energy level in the band gap of germanium was detected, which was suggested to stem from dislocations.<sup>[27]</sup> For deformed ZnO crystals, a bulk photoconductivity was found, in contrast to undeformed samples.<sup>[28]</sup> Dislocations in GaN were demonstrated to act as nonradiative recombination centers leading to a reduction of luminescence intensity.<sup>[29]</sup> Recently, a band gap narrowing has been revealed for ZnS in the dislocation core region after deformation.<sup>[6]</sup> This shifts the absorption edge into the visible light range and could be beneficial for photoelectric applications. Further studies focusing on photoelectric properties of ordered dislocations are still missing in literature, particularly for the class of oxide semiconductors.

Here, we employ macroscopic plastic deformation both at room temperature and at high temperature of Fe-doped strontium titanate single crystals as means to contrast highly aligned dislocations and more randomly distributed dislocation networks. These two mesoscopic structures are compared both locally using conductive atomic force microscopy (C-AFM) and macroscopically applying microelectrodes with a

dependence both on temperature as well as employed exciting wavelength, revealing that ordered dislocations in Fe-doped strontium titanate are not detrimental but can enhance the photoconductivity by orders of magnitude. Furthermore, first evidence will be provided, elucidating a bulk photovoltaic-like response originating from the strain field around the dislocations.

## 2. Results and Discussions

Mechanical deformation of Fe-doped (0.05% wt.) SrTiO<sub>3</sub> single crystals with uniaxial load and by using a stress concentration generated two types of mesoscopic dislocation structures (see **Figure 1** and the Experimental Section). The first type is the result of a room temperature deformation along the [001] direction activating the  $\langle 110 \rangle \{110\}$  slip system (Figure 1a). Hereby,  $\langle \rangle$  denotes a set of crystallographic slip directions corresponding to the Burgers vector, and  $\{ \}$  denotes a set of slip planes.<sup>[1]</sup> This process develops dislocations arranged in parallel slip bands with a dislocation density of about  $2 \times 10^{13} \text{ m}^{-2}$  within the band, corresponding to an average spacing between two dislocations of about 225 nm (Figure 1b). The second slip system is obtained by high temperature (1050 °C) deformation along the crystallographic [110] direction (Figure 1e). This activates the  $\langle 100 \rangle \{100\}$  slip system and yields homogeneously distributed dislocations with a density of  $\approx 10^{12} \text{ m}^{-2}$ , corresponding to an average spacing of 1  $\mu\text{m}$  (Figure 1d).<sup>[19]</sup>

These mechanically introduced dislocations of both slip systems have varying line vector directions leading to screw

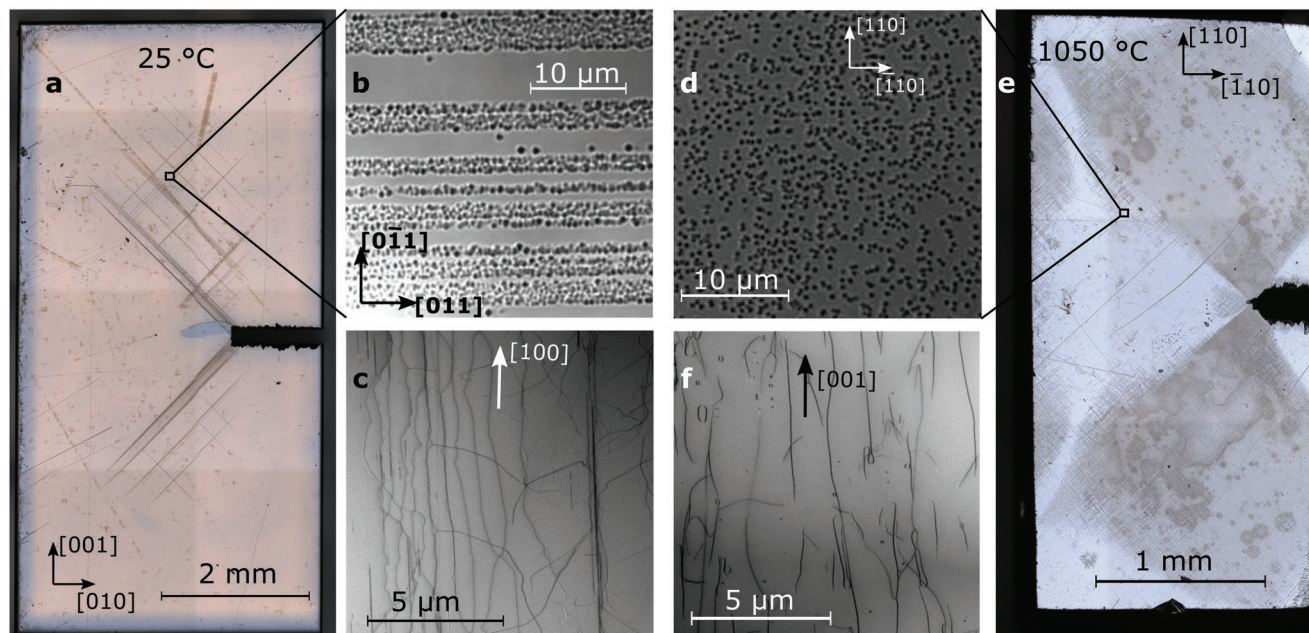


**Figure 1.** Comparison of two mesoscopic dislocation structures. a) Optical microscope image of a [001] oriented SrTiO<sub>3</sub> single crystal deformed at 25 °C. b) SEM image of etch pits revealing individual dislocations of the  $\langle 110 \rangle \{110\}$  slip system arranged in slip bands (see ref. [19]). c) TEM image of the dislocation lines of the  $\langle 110 \rangle \{110\}$  slip system. The indicated [100] direction is perpendicular to the plane provided in (b). d) SEM image of etch pits revealing individual dislocations of the  $\langle 100 \rangle \{100\}$  slip system (see ref. [19]). e) Optical microscope image of a [110] oriented SrTiO<sub>3</sub> single crystal deformed at 1050 °C. f) TEM image featuring elongated dislocation loops of the  $\langle 100 \rangle \{100\}$  slip system form. The indicated [001] direction is perpendicular to the plane depicted in (d).

character in some places and mixed or edge character in other places.<sup>[19]</sup> Thus, they cannot be assigned to pure edge or screw character, as shown by the transmission electron microscope (TEM) investigations in Figure 1c,f. Detailed information about the two dislocation arrangements investigated in this work as well as about mechanics of dislocations in ceramics can be found in ref. [30].

### 2.1. Nanoscale Photoconductivity around Dislocations

AFM/C-AFM investigations on samples of about 700  $\mu\text{m}$  thickness extracted from the deformed crystals allowed correlating the dislocation arrangements with their nanoscale photoelectric properties. The dislocation line vectors (Figure 1c,f) within the samples lie approximately perpendicular to the surface (see Figure 5 in the Experimental Section). To avoid any topography crosstalk in local AFM-based measurements and enable direct correlation of the local properties with dislocation position, the sample surface was patterned in stripe-like regions using photolithography and chemical etching (see the Experimental Section).<sup>[18]</sup>

The surface topography and photocurrent (Figure 2) were measured using a custom-designed photoelectric AFM/C-AFM system. Topography scans in Figure 2a,c visualize the mesoscopic dislocation structures revealed by the dark etch pits in the lower part. As expected, the dislocations of the  $\langle 110 \rangle \{ 110 \}$  slip system are arranged in well-ordered slip bands (Figure 2a). The position of the slip bands in the adjacent

unetched region can be unambiguously deduced from the arrangement of the etch pits in the lower part of the topography scan. The same holds for the dislocations of the  $\langle 100 \rangle \{ 100 \}$  slip system, which are homogeneously distributed (Figure 2c). In this context, it needs to be mentioned that the dislocation density of pristine undeformed crystals is around  $10^8\text{--}10^9\text{ m}^{-2}$ ,<sup>[31]</sup> which corresponds to an average distance between two dislocations in the order of 20  $\mu\text{m}$ . Hence, an undeformed crystal would statistically feature less than one dislocation in the areas similar to the AFM-investigated areas shown in Figure 2. The areas in-between the slip bands have experienced virtually zero deformation and thus, it can be regarded as pristine.

The photocurrent AFM maps reveal significantly higher photoconductivity around the dislocation cores compared to dislocation-free, i.e., pristine, regions. In the upper part of Figure 2b, lines with an up to fourfold increased photocurrent show up. They belong unambiguously to the slip bands of the  $\langle 110 \rangle \{ 110 \}$  slip system (see Figure 2a). A similar observation is valid for homogeneously distributed dislocations of the  $\langle 100 \rangle \{ 100 \}$  slip system (Figure 2c). Here, the maximum current is observed in a dislocation-rich region as well, which can be deduced from the adjacent etched part of the surface (see Figure 2c,d). In the upper right area of the corresponding photocurrent image (Figure 2d), further lines of increased current can be observed. These have a  $45^\circ$  orientation with respect to the  $\langle 110 \rangle$  directions and hence are parallel to the crystallographic  $\langle 100 \rangle$  direction. These can be attributed to aligned dislocations of the  $\langle 100 \rangle \{ 100 \}$  slip system.

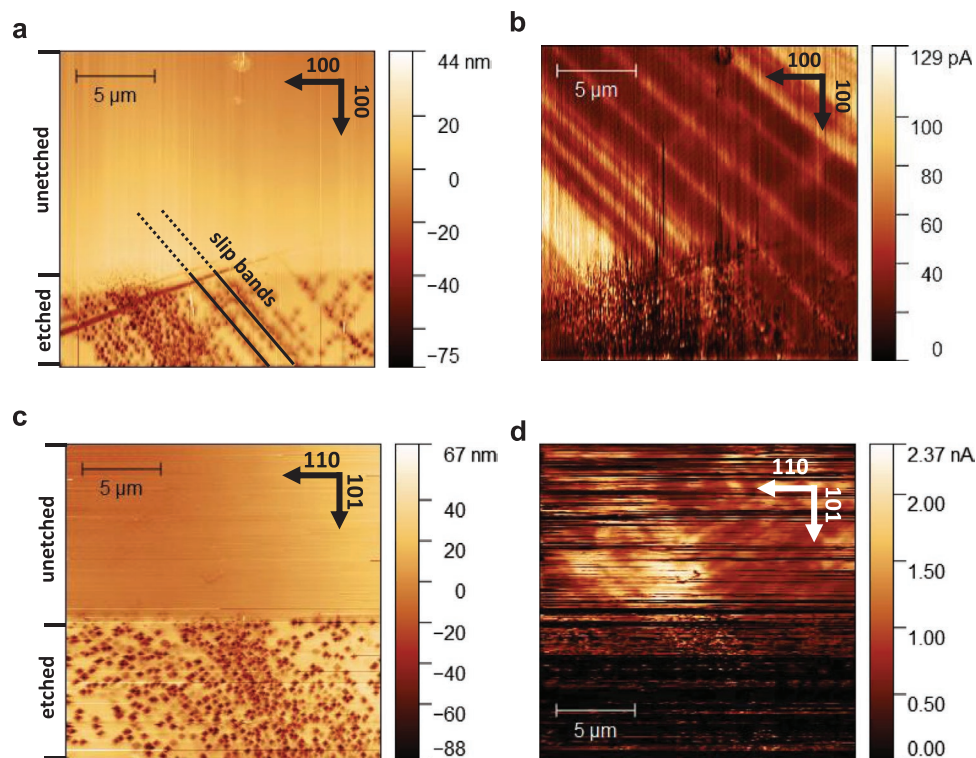


**Figure 2.** Locally enhanced photoconductivity in dislocation-rich regions revealed by local photoelectric characterization. a) Topography image revealing the slip bands of the  $\langle 110 \rangle \{ 110 \}$  slip system in  $\text{SrTiO}_3$  and the smooth, nonetched area; b) the corresponding photocurrent quantified at 20 V applied voltage; c) topography image, similar to (a), of a sample with the  $\langle 100 \rangle \{ 100 \}$  slip system and the corresponding photocurrent d) acquired at 10 V applied voltage.

The higher photoconductivity around the dislocation cores can be attributed to either an enhanced mobility or density of free charge carriers. If the photo-carrier generation and thus the charge carrier density are increased around dislocations, this could result from a band gap narrowing within the dislocation region. This would allow a higher band–band transition rate and was observed for ZnS.<sup>[6]</sup> Furthermore, additional electronic states within the bandgap could be induced by dislocations, which allow for more electronic trap/impurity-band transitions. The latter was suggested to be the case for both dislocation-enhanced photo-response in ZnSe<sup>[25]</sup> and germanium.<sup>[27]</sup>

Charge carrier mobility derived locally can give us first insights into the mechanisms. We can estimate the carrier mobility  $\mu$  considering the fundamental relationship between effective diffusion length, diffusion coefficient  $D$ , and effective bulk lifetime  $\tau$ <sup>[32]</sup>

$$D = \frac{L_D^2}{\tau} = \mu \frac{k_B T}{q} \quad (1)$$

hereby,  $T$  denotes the temperature,  $k_B$  the Boltzmann constant, and  $q$  denotes the elemental charge. The effective diffusion length  $L_D$  is related to the above contrast in photoconductivity within a certain diameter around the dislocation core. For estimation purposes, the peaks in the photocurrent profile perpendicular to the lines with increased photocurrent in Figure 2b were evaluated with a Gaussian fit. This yields a full-width at half-maximum (FWHM) of about 120 nm. This value is significantly larger than the expected spatial resolution of the AFM-based measurement which is in the range of tip-sample contact radius of about 25 nm. Thus, it can be assimilated as a value for the photo-carrier diffusion length. Suppose we compare this value to the typical dislocation core diameter and space charge width. The core extends only by one or two unit cells,<sup>[33]</sup> and the space charge zone width is in the range of a few nanometers up to several tens of nanometers, depending on exact doping density.<sup>[9,34]</sup> This means that the area exhibiting high photocurrent is expected to exceed the core area and space charge zone, which can be rationalized by correlating this region to the diffusion of photo-generated carriers.

We further assume that the effective carrier lifetime is not massively affected by the mechanical boundary conditions and remains within the same order of magnitude.<sup>[35]</sup> It is possible to conservatively estimate the photocarrier mobility by taking the FWHM of the region with increased photoconductivity as an upper limit for the diffusion length. Considering a value as previously reported for the carrier lifetime in the range of 0.5–1 ns,<sup>[36]</sup> the calculated carrier mobility, according to Equation (1), would be in the range of 5–11 cm<sup>2</sup> V<sup>-1</sup> s<sup>-1</sup> which is similar to mobility values determined from classical transport measurements.<sup>[37]</sup> Based on this estimation, the charge carrier mobility does not seem to be increased around dislocations. Thus, it points toward a higher generation rate of charge carriers around the dislocation core and photocarrier diffusion processes away from the core as the main mechanism behind the local enhancement of the photoconductivity, which will be discussed in the following.

## 2.2. Macroscopic Photoresponse of Dislocation Arrangements

Macroscale in-plane measurements using patterned micro-contacts were performed on the same samples to analyze the effect of dislocations on the global macroscopic photoresponse. This should lead to a better understanding of the origin of the enhanced photoconductivity around the dislocation core. To this end, the spectral photoresponse in the wavelength range between 325 and 700 nm at different temperatures between 85 and 300 K was evaluated. For the  $\langle 110 \rangle \{ 110 \}$  slip system arranged in slip bands, the photocurrent was quantified in-plane along the direction of these bands. This means perpendicular orientation to the line vectors, i.e., parallel to the crystallographic  $\langle 110 \rangle$  direction, by using patterned electrodes in designated areas (see Figure 5c,d in the Experimental Section). An undeformed sample processed in the same conditions served as reference.

A massive increase in photoconductivity of the  $\langle 110 \rangle \{ 110 \}$  slip system compared to the pristine sample can be observed at almost all temperatures. Figure 3a–c depicts the spectral response of the photoconductivity in exemplary fashion at two different temperatures, room temperature and 150 K, respectively.

The onset in photoconductivity, which is directly related to band-to-band electronic transitions, occurs for all samples at about 385 nm, corresponding to a band gap of 3.2 eV. This band gap value correlates well with literature in SrTiO<sub>3</sub>.<sup>[38]</sup> Hence, the high density of dislocations apparently does not affect the band gap, as in the case of ZnS.<sup>[6]</sup>

Furthermore, at photon energies well below the band gap, corresponding to the wavelength range between 550 and 700 nm, a significant photoconductive signal is detected for the  $\langle 110 \rangle \{ 110 \}$  slip system without distinct peaks (Figure 3b,c). This is an indication of additional energy levels in the forbidden gap. However, as this effect is also noted in nondeformed samples, it cannot be directly attributed to dislocation formation.<sup>[27]</sup>

In contrast, the  $\langle 100 \rangle \{ 100 \}$  slip system features significantly lower in-plane photoconductivity with no detectable photoconductivity contribution in the long-wavelength regime (see Figure 3b,c). This missing sub-band gap response is a clear indication that the two slip systems result in a different global electronic behavior despite a similar local enhancement.

For both slip systems, the spectral photoresponse measurements do not indicate a massive contribution of the intraband gap levels, as in the case of germanium or ZnSe pointing to genuine increase of the generation rate around dislocations, as observed in Figure 2.

The temperature dependence of the macroscopic in-plane photoconductivity strongly confirms the dissimilar behavior of the two slip systems. Figure 3d displays the temperature evolution of above band gap photoconductivity measured at 330 nm. It reveals a strong temperature dependence with maximum photoconductivity between 200 and 250 K for the sample with the  $\langle 110 \rangle \{ 110 \}$  dislocations and the pristine sample. The photoconductivity of the slip bands increases at least one order of magnitude compared to the pristine sample. That is valid for almost the entire temperature range. Note that a similar temperature dependence was observed in other wide band gap semiconductors such as GaN.<sup>[39,40]</sup> This might be related to different dominant scattering mechanisms.

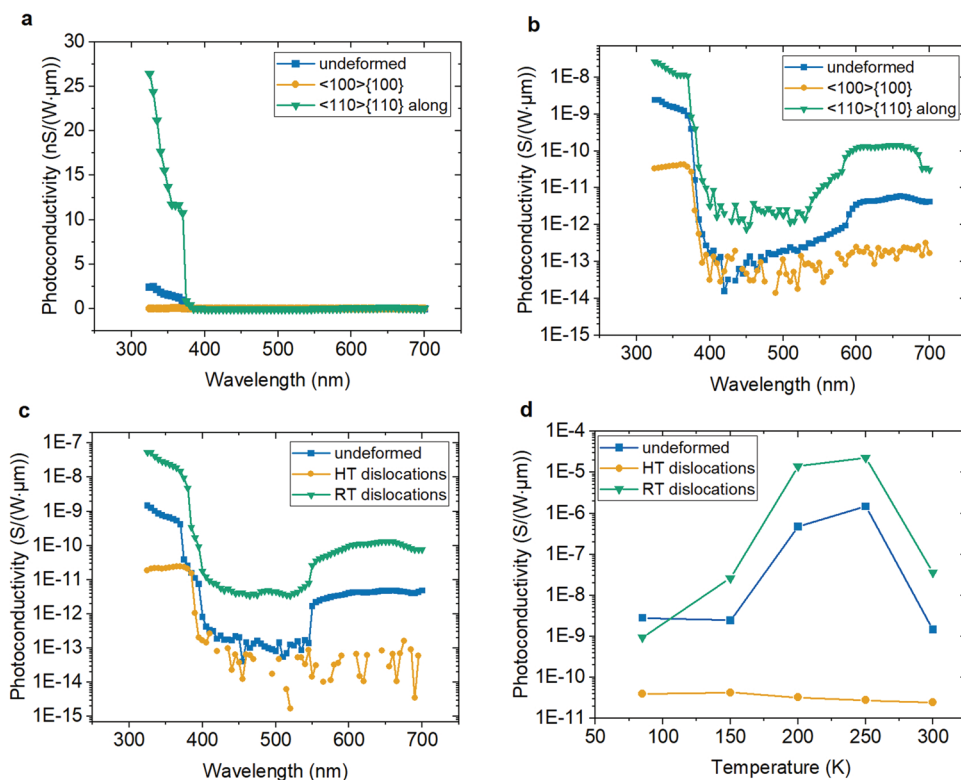


**Figure 3.** Wavelength dependence of macroscopic photoconductivity measured at 150 K in a) linear and b) logarithmic scale, respectively, and measured at c) 300 K; d) above band gap photoconductivity ( $\lambda = 330$  nm) as a function of temperature.

In contrast, the  $\langle 100 \rangle \{100\}$  slip system is characterized by a dramatically reduced photoconductivity even compared to the pristine sample. The difference between the two slip systems is about four orders of magnitude in photoconductivity at room temperature and increases up to six orders of magnitude in the 200–250 K range. Additionally, the  $\langle 100 \rangle \{100\}$  slip system does not exhibit a strong temperature dependence.

The missing temperature dependence and the absence of the sub-band gap response are two characteristics of the  $\langle 100 \rangle \{100\}$  slip system. They may be the result of an annealing effect since only the  $\langle 100 \rangle \{100\}$  slip system was fabricated using a temperature of 1050 °C. Thereby, the respective electronic states can be rendered inactive or change the character toward recombination levels. These extended effects are not activated in  $\langle 110 \rangle \{110\}$  slip system nor the pristine sample, which were prepared at room temperature.

### 2.3. Comparison between Nanoscale and Macroscale Observations

The macroscale photoresponse of the two slip systems is in variance with the previously discussed nanoscale C-AFM measurements. While dislocations of both slip systems exhibit significantly higher local photoconductivity, an increase in macroscopic photoconductivity was only found for the  $\langle 110 \rangle \{110\}$  slip system.

We attribute these observations mainly to the different measurement directions combined with the different mesoscopic

dislocation structures (see Figure 5 in the Experimental Section). In AFM-based local characterization, the photocurrent is quantified out-of-plane along the dislocation lines. In contrast, during the macroscopic measurements, the current is measured in-plane as a collective response of multiple dislocations. Hereby, the formation of conductive pathways is required, which is related to the overlapping of photoconductive regions around the dislocation cores, controlled by the mesoscopic dislocation structure.

For the  $\langle 110 \rangle \{110\}$  slip system, the dislocations feature narrow spacing over long distances (see also Figure 1b,c). A percolating path along the slip bands can form, and, therefore, the locally enhanced conductivity directly translates into the enhancement at macroscale.

In contrast, the dislocations of the  $\langle 100 \rangle \{100\}$  slip system do not affect the macroscopic photoconductivity despite a local enhancement. The dislocations are all elongated loops (see also Figure 1f) with large average distances and a broad distribution of spacing between them (see Figure 1d). Thus, the formation of a percolating network of enhanced photoconductivity is prohibited and ultimately also leads to a blocking effect with lower photoconductivity than in a pristine sample. This observation of the impact of dislocation arrangement on local and macroscopic behavior is in accordance with similar results in titania.<sup>[10]</sup>

For both slip systems, the local measurements revealed a strong increase in photoconductivity around the dislocation cores, significantly exceeding the regular bulk response. Our investigations do not prove an increased charge carrier mobility

or increased intraband levels that could explain the enhanced photoconductivity. Hence, the detailed mechanism of this effect still remains to be established.

It may indeed be a higher generation rate at the dislocation cores themselves due to additional states generated during deformation and dislocations moving by the so-called sweeping up mechanisms.<sup>[41]</sup> This mechanism describes the movement of dislocations through a large lattice volume, thereby gathering impurities and segregating them at the charged core, thus generating additional defect levels at the dislocation. These defect levels may actually have a certain energy distribution across the band gap and thus cannot be resolved as distinct peaks in the spectral photoresponse.

Alternatively, the local strain and symmetry breaking may enhance the mobility in the vicinity of the dislocation core in SrTiO<sub>3</sub>.<sup>[42]</sup> This would be completely different than in classical semiconductors such as GaN, where edge dislocations act as additional scattering centers reducing the electron mobility.<sup>[40]</sup>

Owing to the fact that locally increased photoconductivity translates into the enhancement at the macroscale only in the case of the  $\langle 110 \rangle \{ 110 \}$  slip system stresses the importance of the mesoscopic dislocation arrangements as a key design parameter for functional properties. The drastic reduction of the in-plane photoconductivity in the  $\langle 100 \rangle \{ 100 \}$  slip system, also compared to the pristine sample, may point to a very complex strain-free carrier interaction that must be in detail investigated.

#### 2.4. Outlook: Indications of a Bulk-Photovoltaic-Like Signal

The slip bands of the  $\langle 110 \rangle \{ 110 \}$  slip system do not only exhibit higher photoconductivity but also a bulk photovoltaic (PV) signal, respectively, a substantial photo-generated current under zero bias. The corresponding macroscopic spectral photo-response measured at room temperature is depicted in **Figure 4a**. The PV response has not been detected in the  $\langle 100 \rangle \{ 100 \}$  slip system nor the pristine SrTiO<sub>3</sub> sample using similar electrodes. To prove that this is a bulk-like PV signal, the PV current was quantified as a function of the light polarization angle, which describes the angle between the plane of the linearly polarized light and the optical axis of the half-wave plate. A typical

cosine dependence<sup>[43,44]</sup> has been observed (see **Figure 4b**), with an amplitude being around 4% as compared to the mean total photocurrent.

A photocurrent under zero bias and a periodic dependence on the angle between the PV current and the light polarization are two main ingredients characteristic for the bulk photovoltaic (BPV) effect.<sup>[43,41]</sup> The BPV is typically found in noncentrosymmetric materials and is not characteristic of pristine centrosymmetric SrTiO<sub>3</sub>. However, the large strain gradients carried by dislocations are asymmetrically distributed around the cores.<sup>[45]</sup> This can locally break the inversion symmetry, leading to both flexoelectric polarization<sup>[20,46]</sup> and potentially enabling the BPV, which has been reported as flexo-photovoltaic effect (FPV).<sup>[21]</sup> We hypothesize that the mechanism behind the PV signal (**Figure 4**) is the FPV induced through the strain fields of dislocations and the local break of the inversion symmetry.

Nevertheless, the measured light polarization dependence displayed in **Figure 4b** is small compared to the total photocurrent and differs substantially from regular dependence observed for innate non-centrosymmetric materials.<sup>[47]</sup> For the latter, the dependence can be mathematically described by a simple sinusoidal function, whereas this has a much more complex behavior in the dislocation-based system. We may attribute this to a rather complex spatial distribution of strain and its gradients around dislocations.<sup>[45]</sup> Dislocations can have changing line vector directions and varying vicinity with asymmetrically distributed neighboring dislocations.<sup>[19,48]</sup> This may lead to a more complex dependence than a simple sinusoidal function. Furthermore, the effects of individual dislocations may partially compensate, resulting in a lowering of the effective photocurrent amplitude.

### 3. Conclusion

Dislocations can boost the photoconductivity in oxide semiconductors. This was illustrated on well-ordered, high-density dislocation structures, produced in Fe-doped SrTiO<sub>3</sub> single crystals. AFM-based local photoconductivity measurements demonstrated that the regions around dislocation cores of both  $\langle 100 \rangle \{ 100 \}$  and  $\langle 110 \rangle \{ 110 \}$  slip systems exhibit an up to four-fold increased photoconductivity compared to the dislocation

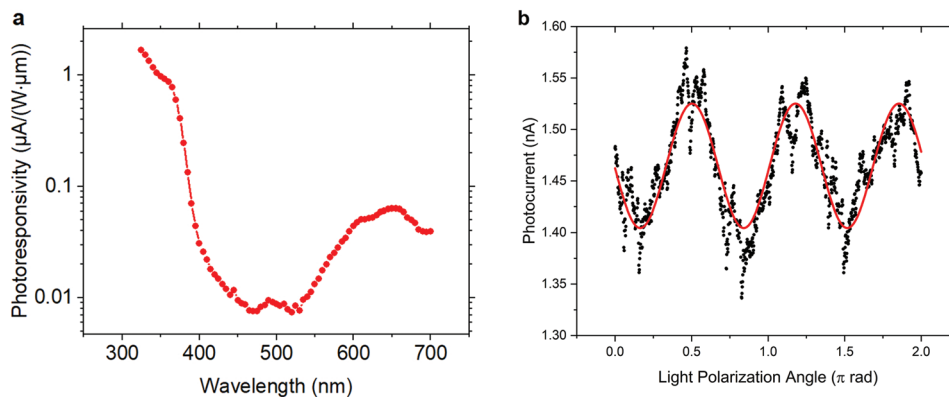


**Figure 4.** Indications of a bulk photovoltaic effect at room temperature. a) Spectral response of the photovoltaic signal ( $U_{\text{applied}} = 0$  V) measured along a slip band of the  $\langle 110 \rangle \{ 110 \}$  slip system. b) Photocurrent dependence on light polarization angle at 375 nm laser illumination. The red line in (b) is a fit with a sinusoidal function.

free regions of the sample. The estimated photo-generated charge carriers possess a diffusion length of about 120 nm which yields an effective mobility value of 5–11 cm<sup>2</sup> V<sup>-1</sup> s<sup>-1</sup> at room temperature. Additional in-plane surface measurements with microcontacts along the dislocation slip bands reveal a by orders of magnitude increased global photoconductivity for the ⟨110⟩{110} slip system as compared to a pristine sample. On the contrary, in the case of the ⟨100⟩{100} slip system, the macroscopic photoconductivity decreases by orders of magnitude at all photon energies. These differences were rationalized with the mesoscopic dislocation structures affecting the ability to form a macroscopically percolating photoconductive path.

The orders of magnitude enhancement of the local photoconductivity along the dislocation core and in-plane for a certain crystallographic slip system prove unambiguously that dislocations in oxide semiconductors are beneficial for certain functional properties and can offer potential routes for future 1D devices. The observed indications of a bulk-photovoltaic signal which are potentially based on the flexo-photovoltaic effect, foreshadow the ability of new dislocation-engineered functionalities.

#### 4. Experimental Section

**Sample Preparation:** Ordered dislocation structures were introduced by mechanical deformation in acceptor-doped Fe-SrTiO<sub>3</sub> (0.05% wt.) single crystals, 4 mm × 4 mm × 8 mm, (Alineason Materials Technology GmbH) of which the crystal faces corresponded to the {100} planes (see Figure 1). The controlled acceptor of Fe doping was for the overall electronic properties net superior to undoped crystals. The latter still contained impurities of varying and unknown amounts, which acted

as doping and made reliable electronic investigations practically impossible.

For the high-temperature deformation, smaller specimens were cut out of the delivered samples. In these specimens of a size of 4 × 1.8 × 1.9 mm<sup>3</sup>, the [110] axis was the long axis along which the crystal was deformed. The single crystals were notched with a 170 μm thick diamond wire saw (Well 4240, Well Diamantdrahtsägen GmbH) in order to provide a stress concentration activating only two slip systems. The notch depth was between 15% and 25% of the sample's thickness.

Afterward, dislocations were introduced by plastic deformation under uniaxial compression (Z010, Zwick GmbH) at room temperature along [001] and at 1050 °C along [110].<sup>[19]</sup> A displacement of 8 μm along the [001] direction was attained at room temperature under a load of 1200 N, activating the ⟨110⟩{110} slip system. Dislocations were developed and arranged within parallel slip bands along the crystallographic ⟨110⟩ directions. The dislocation density achieved in the band was around 2 × 10<sup>13</sup> m<sup>-2</sup>, corresponding to an average distance of 225 nm between the dislocations. Holding a load of 950 N resulted in a displacement of 40 μm along the [110] direction at 1050 °C, activating the ⟨100⟩{100} slip system. The dislocations were homogeneously distributed throughout the sample leading to a density of ≈10<sup>12</sup> m<sup>-2</sup> which corresponded to an average distance between the dislocations of 1 μm.

The deformed cuboid samples were cut into small slices with a thickness of ≈700 μm. The cutting was done in a way that the dislocation lines went through the thickness of the slices (see Figure 5a,b). The surface of the slices was ground using P1200, P2500, and P4000 SiC sandpaper to achieve plane-parallel surfaces. Mechanical polishing was done automatically with a polishing machine (Phoenix 4000, Jean Wirtz GmbH), followed by vibrational polishing.

Dislocation position, arrangement, and density were revealed by etching, i.e., by forming etch pits. To avoid any interference of the AFM-tip with topography of the etch pits during the measurements, the surface was partly etched in form of a stripe pattern (see Figure 5c). To this end, a polymer stripe-like mask (ma-N 1440, micro-resist technology) was placed onto the sample via photolithography. The open stripes were etched with a solution of 16 drops of 50% HF (H<sub>2</sub>O) in 15 mL of 50%

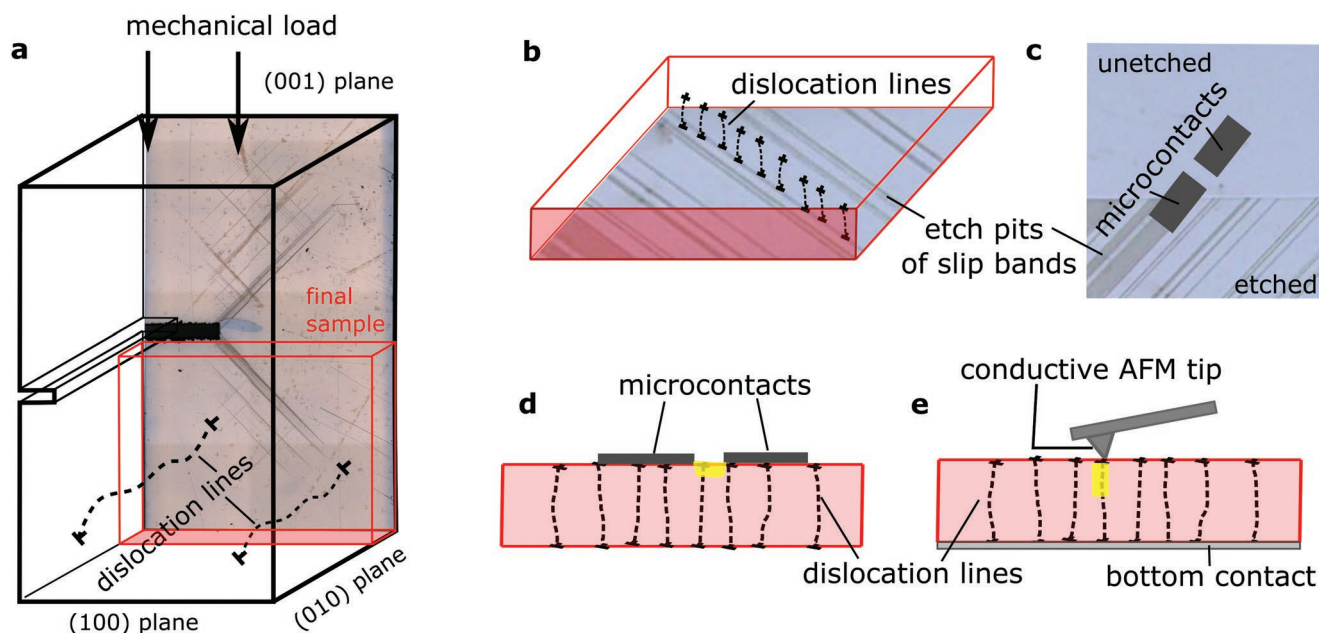


**Figure 5.** Orientation of dislocations in deformed SrTiO<sub>3</sub> single crystals. a) Sketch indicating the orientation of the final sample slice with respect to the crystal and the dislocation lines. b) Dislocation lines extend from top to bottom of the slices. End of dislocation lines are visible on the surface by forming etch pits. c) Microcontacts are oriented on the stripe-etched surface to measure the current along the slip bands but within the nonetched area. d) Microcontacts detect the in-plane surface current (yellow). e) The conductive AFM tip records the out-of-plane current (yellow) which is flowing along the dislocation lines.

HNO<sub>3</sub> (H<sub>2</sub>O) for about 1 min. The nonetched regions, protected by the photoresist, retained the polished surface quality, respectively, ≈2 nm root mean squared roughness. The position of the dislocations in these regions could be deduced from the adjacent etched regions.

The stripes on the sample with dislocations of the ⟨110⟩{110} slip system were 95 μm (etched) and 155 μm (unetched) wide, whereas for the sample with dislocations of the ⟨100⟩{100} slip system, they were 40 μm (etched) and 60 μm (unetched). The samples were finally annealed for 18 h at 750 °C under forming gas (95% N<sub>2</sub>; 5% H<sub>2</sub>) to increase the base electrical conductivity.

**Structural and Photoelectric Measurements:** For the TEM experiments, one sample was cut at a 2° angle to the slip plane both for the SrTiO<sub>3</sub> single crystals deformed at room temperature and at 1050 °C. The samples were thinned by conventional polishing and ion milling. The acceleration voltage was set to 1 MeV in BF-STEM mode using the JEOL JEM-1000k RS at Nagoya University.

Local AFM and photoelectric measurements were performed using a ThermoMicroscope AutoProbe CPIX provided with Pt/Ir coated Si-tips (Nanosensors, PPP-EFM). Uniform illumination from a UV laser photodiode with a wavelength of 375 nm ( $h\nu = 3.3$  eV) and a power density of about 1.5 W cm<sup>-2</sup> was employed. The out-of-plane currents were recorded under an applied bias voltage of 10 and 20 V between the tip and silver paste as bottom contact (see Figure 5e). The signals collected by the AFM tip were amplified by a trans-impedance amplifier (DLPCA-200, Femto) with variable gain of 10<sup>5</sup>–10<sup>8</sup> V A<sup>-1</sup> and a typical bandwidth of 400 kHz. The current signal was then fed into an auxiliary input of the microscope and simultaneously mapped with the topography.

For the macroscopic measurements Ti-Au electrodes (150 μm long and 20 μm gap in-between) were patterned on nonetched, i.e., pristine polished, stripes of the samples. In case of the sample with the ⟨110⟩{110} dislocations, they were optically aligned with the slip bands so that the current was measured along these bands (see Figure 5c). For the sample with homogeneously distributed ⟨100⟩{100} dislocations and the pristine reference sample, no specific alignment was applied. Spectral and temperature dependence of in-plane surface photocurrents (see Figure 5d) were measured with samples mounted in a cryostat (Janis VPF-700) using an electrometer (Keithley 6517B) and a spectral light source comprising a 250 W Xe lamp and a monochromator (Oriel 74004). The spectral power density at the measuring stage was recorded using a calibrated Si photodiode (Newport 818UV). All currents were normalized to the spectral power density.

The photovoltaic signal was obtained using a UV laser diode (375 nm). The light polarization was varied using a half-wave plate and a motorized rotating stage (ThorLabs).

## Acknowledgements

The financial support by the Engineering and Physical Science Research Council (EPSRC) EP/T027207/1 and EP/P025803/1 is gratefully acknowledged. M.A. acknowledges the Alexander von Humboldt Research Award. The work was supported by project no. 414179371 of the German Research Foundation (DFG).

## Conflict of Interest

The authors declare no conflict of interest.

## Author Contributions

M.A. conceived the idea, M.K. prepared the samples with the assistance of L.P. and conducted and analyzed the AFM and macroscopic photoelectric measurements, A.N. provided the TEM observations, L.P., T.F., and J.R. contributed to the discussion. All authors contributed to the manuscript writing.

## Data Availability Statement

The data that support the findings of this study are available from the corresponding author upon reasonable request.

## Keywords

conductive atomic force microscope, dislocations, microelectrodes, oxide ceramic single crystals, photoconductivity, photovoltaic effect

Received: April 3, 2022

Revised: May 31, 2022

Published online: July 10, 2022

- [1] K. Szot, C. Rodenbücher, G. Bihlmayer, W. Speier, R. Ishikawa, N. Shibata, Y. Ikuhara, *Crystals* **2018**, *8*, 241.
- [2] Y. Furushima, A. Nakamura, E. Tochigi, Y. Ikuhara, K. Toyoura, K. Matsunaga, *J. Appl. Phys.* **2016**, *120*, 142107.
- [3] H.-S. Lee, T. Mizoguchi, J. Mistui, T. Yamamoto, S.-J. L. Kang, Y. Ikuhara, *Phys. Rev. B* **2011**, *83*, 104110.
- [4] J. Amodeo, S. Merkel, C. Tromas, P. Carrez, S. Korte-Kerzel, P. Cordier, J. Chevalier, *Crystals* **2018**, *8*, 240.
- [5] P. Gumbsch, S. Taeri-Baghadrani, D. Brunner, W. Sigle, M. Rühle, *Phys. Rev. Lett.* **2001**, *87*, 085505.
- [6] Y. Oshima, A. Nakamura, K. Matsunaga, *Science* **2018**, *360*, 772.
- [7] Y. Oshima, A. Nakamura, K. P. D. Lagerlöf, T. Yokoi, K. Matsunaga, *Acta Mater.* **2020**, *195*, 690.
- [8] R. W. Whitworth, *Adv. Phys.* **1975**, *24*, 203.
- [9] K. K. Adepalli, J. Yang, J. Maier, H. L. Tuller, B. Yildiz, *Adv. Funct. Mater.* **2017**, *27*, 1700243.
- [10] Q. K. Muhammad, L. Porz, A. Nakamura, K. Matsunaga, M. Rohnke, J. Janek, J. Rödel, T. Frömling, *Nano Energy* **2021**, *85*, 105944.
- [11] B. Yildiz, *MRS Bull.* **2014**, *39*, 147.
- [12] J. M. Börgers, J. Kler, K. Ran, E. Larenz, T. E. Weirich, R. Dittmann, R. A. De Souza, *Adv. Funct. Mater.* **2021**, *31*, 2105647.
- [13] K. Szot, W. Speier, G. Bihlmayer, R. Waser, *Nat. Mater.* **2006**, *5*, 312.
- [14] P. Ren, M. Song, J. Lee, J. Zheng, Z. Lu, M. Engelhard, X. Yang, X. Li, D. Kisailus, D. Li, *Adv. Mater. Interfaces* **2019**, *6*, 1901121.
- [15] M. Höfling, X. Zhou, L. M. Riemer, E. Bruder, B. Liu, L. Zhou, P. B. Groszewicz, F. Zhuo, B. Xu, K. Durst, X. Tan, *Science (1979)* **2021**, *372*, 961.
- [16] S. Hameed, D. Pelc, Z. W. Anderson, A. Klein, R. J. Spieker, L. Yue, B. Das, J. Ramberger, M. Lukas, Y. Liu, M. J. Krogstad, R. Osborn, Y. Li, C. Leighton, R. M. Fernandes, M. Greven, *Nat. Mater.* **2021**, *21*, 54.
- [17] D. Marrocchelli, L. Sun, B. Yildiz, *J. Am. Chem. Soc.* **2015**, *137*, 4735.
- [18] P. Gao, R. Ishikawa, B. Feng, A. Kumamoto, N. Shibata, Y. Ikuhara, *Ultramicroscopy* **2018**, *184*, 217.
- [19] L. Porz, T. Frömling, A. Nakamura, N. Li, R. Maruyama, K. Matsunaga, P. Gao, H. Simons, C. Dietz, M. Rohnke, J. Janek, J. Rödel, *ACS Nano* **2020**, *15*, 9355.
- [20] P. Gao, S. Yang, R. Ishikawa, N. Li, B. Feng, A. Kumamoto, N. Shibata, P. Yu, Y. Ikuhara, *Phys. Rev. Lett.* **2018**, *120*, 267601.
- [21] M. M. Yang, D. J. Kim, M. Alexe, *Science (1979)* **2018**, *360*, 904.
- [22] Y. A. Osipyan, V. F. Petrenko, A. V. Zaretskii, R. W. Whitworth, *Adv. Phys.* **1986**, *35*, 115.
- [23] A. V. Zaretskii, V. F. Petrenko, *Fiz. Tverd. Tela* **1978**, *20*, 1167.
- [24] A. V. Zaretskii, V. F. Petrenko, *Fiz. Tverd. Tela* **1983**, *25*, 532.
- [25] L. G. Kirichenko, V. F. Petrenko, *Sov. Phys., Solid State* **1980**, *22*, 929.



- [26] L. Kirichenko, V. F. Petrenko, G. V. Uimin, *J. Exp. Theor. Phys.* **1978**, 47, 389.
- [27] R. Labusch, J. Hess, *Phys. Status Solidi A* **1994**, 146, 145.
- [28] L. Carlsson, C. Svensson, *J. Appl. Phys.* **1970**, 41, 1652.
- [29] I. Yonenaga, Y. Ohno, T. Yao, K. Edagawa, *J. Cryst. Growth* **2014**, 403, 72.
- [30] L. Porz, *Mechanics and Electrical Conductivity of Dislocation-Tuned Ceramics*, Technische Universität Darmstadt, Darmstadt, Germany **2021**.
- [31] E. A. Patterson, M. Major, W. Donner, K. Durst, K. G. Webber, J. Rödel, *J. Am. Ceram. Soc.* **2016**, 99, 3411.
- [32] S. M. Sze, *Physics of Semiconductor Devices*, John Wiley and Sons, New York **1981**.
- [33] W. Sigle, C. Sarbu, D. Brunner, M. Rühle, *Philos. Mag.* **2006**, 86, 4809.
- [34] K. K. Adepalli, M. Kelsch, R. Merkle, J. Maier, *Adv. Funct. Mater.* **2013**, 23, 1798.
- [35] D. Wrana, T. Gensch, B. R. Jany, K. Cieřlik, C. Rodenbücher, G. Cempura, A. Kruk, F. Krok, *Appl. Surf. Sci.* **2021**, 569, 150909.
- [36] Y. Kanemitsu, Y. Yamada, *Phys. Status Solidi B* **2011**, 248, 416.
- [37] E. Mikheev, B. Himmetoglu, A. P. Kajdos, P. Moetakef, T. A. Cain, C. G. van de Walle, S. Stemmer, *Appl. Phys. Lett.* **2015**, 106, 062102.
- [38] K. van Benthem, C. Elsässer, R. H. French, *J. Appl. Phys.* **2001**, 90, 6156.
- [39] H. M. Ng, D. Doppalapudi, T. D. Moustakas, N. G. Weimann, L. F. Eastman, *Appl. Phys. Lett.* **1998**, 73, 821.
- [40] D. G. Zhao, H. Yang, J. J. Zhu, D. S. Jiang, Z. S. Liu, S. M. Zhang, Y. T. Wang, J. W. Liang, *Appl. Phys. Lett.* **2006**, 89, 3.
- [41] R. W. Whitworth, *Philos. Mag. A* **1985**, 51, 857.
- [42] B. Jalan, S. J. Allen, G. E. Beltz, P. Moetakef, S. Stemmer, *Appl. Phys. Lett.* **2011**, 98, 132102.
- [43] B. I. Sturman, V. M. Fridkin, *The Photovoltaic and Photorefractive Effects in Noncentrosymmetric Materials*, Routledge, London **1992**.
- [44] V. M. Fridkin, *Crystallogr. Rep.* **2001**, 46, 654.
- [45] W. Cai, A. Arsenlis, C. R. Weinberger, V. v. Bulatov, *J. Mech. Phys. Solids* **2006**, 54, 561.
- [46] P. Zubko, G. Catalan, A. K. Tagantsev, *Annu. Rev. Mater. Res.* **2013**, 43, 387.
- [47] V. M. Fridkin, E. P. Efremova, B. H. Karimov, V. A. Kuznezov, I. P. Kuzmina, A. N. Lobachev, V. G. Lazarev, A. J. Rodin, *Appl. Phys.* **1981**, 25, 77.
- [48] L. Porz, A. J. Klomp, X. Fang, N. Li, C. Yildirim, C. Detlefs, E. Bruder, M. Höfling, W. Rheinheimer, E. A. Patterson, P. Gao, K. Durst, A. Nakamura, K. Albe, H. Simons, J. Rödel, L. Porz, *Mater. Horiz.* **2021**, 8, 1528.